Supplemental Information for "Intermittent upwelling events trigger delayed, major, and reproducible pico-nanophytoplankton responses in coastal oligotrophic waters"

R. Fuchs[1,2] *, V. Rossi[2] †, C. Caille[3] ‡, N. Bensoussan[2] §, C. Pinazo[2] ¶, O. Grosso[2] ‖, M. Thyssen[2] ††

[1]Aix Marseille Univ, CNRS, Centrale Marseille, I2M, Marseille, France

[2]Aix Marseille Univ, Université de Toulon, CNRS, IRD, MIO, Marseille, France

[3]Sorbonne Université, CNRS, LOMIC, Banyuls-sur-Mer, France

Contents of this file

1. Material and Methods details

*robin.fuchs@univ-amu.fr

†vincent.rossi@mio.osupytheas.fr

‡caillec@obs-banyuls.fr

§nathaniel.bensoussan@mio.osupytheas.fr

¶christel.pinazo@mio.osupytheas.fr

‖olivier.grosso@mio.osupytheas.fr

†† melilotus.thyssen@mio.osupytheas.fr

2. Figures S1 to S10

3. Tables S1 to S3

1. Materials and Methods Details

1.1. Stratified Period, Bloom Period and Salinity Data

1.1.1. Stratified periods characterization

The stratified period and the temperature anomalies were computed using a Butterworth digital and analog filter design (function butter of the Python "scipy.signal" subpackage). The bandwidth parameter was set to 60 days for the stratified periods determination and 15 days for the temperature anomaly. Events associated with temperature anomalies lasting less than eight hours were not considered.

1.1.2. Spring Bloom Periods Characterization

The dates of the spring bloom were determined using the threshold method (Sapiano et al., 2012; Brody et al., 2013) on the low-pass filtered biomass with a 5% threshold. The dates of the blooms in 2020 were from April 2 to April 30, 2020. There were two spring blooms in 2021, from March 25 to April 7 and from April 21 to May 12 (See Figures S4 and S5).

1.1.3. Salinity Data

The salinity data were acquired every hour using an STPS sensor from the NKE-manufacturer. Yet, salinity measurements from the STPS sensor were found not reliable and hence not used here.

1.2. Estimations of Phytoplankton Biovolume, Biomass and Growth Rates

1.2.1. Phytoplankton functional groups acquisition protocol summary

Phytoplankton organisms present significant differences in typical sizes and abundances (Finkel et al., 2010) so that two AFCM acquisition procedures are used to overcome this issue (as for example in Marrec et al. (2018)). Redpicopro and Orgpicopro pulse shape signals were acquired by setting a low red fluorescence threshold (6 mV) and by analyzing a volume of $850\mu L$ on average whereas the Redpicoeuk, Rednano, and Orgnano pulse shape signals were acquired using a high red fluorescence threshold (25 mV) and by analyzing volumes of $4000\mu L$ on average. The volume analyzed was quantified using a weight-calibrated peristaltic pump.

1.2.2. Biovolume estimation:

The biovolume of each phytoplankton cell was estimated using the relationship between AFCM Total forward scatter (the area under the FWS pulse shape) and the biovolume of Silica Beads and cell images taken by the AFCM (Figure S1). The Silica Beads were manufactured with a known size and the cell biovolumes from images were estimated according to Sun and Liu (2003). Even if the relationship existing between these two quantities is monotonic, its shape seemed not to be constant over all the possible Total FWS values. This pattern is due to the optical properties of the phytoplankton cell sizes relatively to the laser size. Indeed, for the cells exhibiting a Total FWS inferior to 2×10^2 a.u. the relationship seemed concave whereas it was convex for cells with Total FWS superior to 5×10^2 a.u. as made visible in Figure S1.

1.2.3. Biomass estimation:

The biomass of each cell was computed from the estimated biovolume (BV) using the following relationships:

• $Biomass = 0.260 \times BV^{0.860}$ for Redpicopro, Orgpicopro and Redpicoeuk cells according to Menden-Deuer and Lessard (2000).

• $Biomass = 0.433 \times BV^{0.863}$ for Rednano and Orgnano cells according to Verity et al. (1992).

1.3. Size-structured matrix population model

The size-structured model version introduced in Ribalet et al. (2015) was used. The corresponding code is available at `https://github.com/fribalet/ssPopModel` (version 1.1.0). By definition, the model is structured in size and the user has to define the number of classes along with a lower and upper bound of possible size for each PFG. In this study, the distribution of each PFG was discretized in 31 classes. The lower and upper bounds of a PFG size class were determined as the 1 over 1000 quantile and 999 over 1000 quantile of the PFG biovolume distribution during each SWUE, respectively. It prevented integrating outliers and avoided excluding a significant number of observations. The PFG data were linearly interpolated from a two-hour frequency to a one-hour frequency. The lightning data used by the model came from the MESURHO buoy (Cadiou et al., 2010) moored at the Rhone river mouth which is located about 40 kilometers away from the SSL@MM station. It provided the Photosynthetically Available Radiation data (PAR, $\mu E.m^{-2}.s^{-1}$) on a two hours basis. The PAR data were linearly interpolated on a 10 minutes basis. The PAR data were not available in 2021 due to a technical issue on the buoy and the growth rates were only calculated for 2019 and 2020.

1.4. PFG response identification

The rupture detection was conducted thanks to the Python "rupture" package: `https://github.com/deepcharles/ruptures`. A linear cost function with intercept was used to model the link between the water temperature and each PFG abundance or biomass signal. No observation subsampling was performed and a binary segmentation research method was used to minimize the cost function. As the goal was to identify the beginning and end of each PFG reaction, the number of rupture points was known and equal to two.

1.5. Computation of the additional biomass imputable to the Spring Bloom

The additional biomass generated between the start and the end of the bloom was computed by taking the median value over the preceding week before the bloom as a reference value. It was assumed that the biomass would have remained at this level during the whole period if the bloom did not occur. As a result, the daily additional biomass imputable to the bloom was computed as the difference between the actual total integrated biomass and the integrated reference level divided by the bloom duration in days.

2. Wind-driven Upwelling/Downwelling Index

The Wind-driven Upwelling/Downwelling Index is an hourly index that uses the sea surface wind speed and direction to estimate the Ekman transport perpendicular to the coastline (Bakun, 1973). A positive index value implies that surface waters are transported offshore (due to upwelling-favorable winds); conversely, a negative index value indicates that surface waters flow onshore (denoting wind favorable to downwelling events). An

upwelling event is a series of consecutive positive WUDI values. As in Odic, Bensoussan, Pinazo, Taupier-Letage, and Rossi (2022), events with average indices higher than $0.432 m^3.s^{-1}m^{-1}$ were considered as significant upwelling events. These events are associated with substantial changes in surface water temperature (more than 3°C on average, see Odic et al. (2022)), suggesting also measurable responses of both biogeochemistry (nutrients) and biology (phytoplankton). Events are considered distinct if they are separated from each other by at least one day (Millot, 1979).

References

Bakun, A. (1973). Coastal upwelling indices, west coast of north america, 1946-71. *NOAA technical report*.

Brody, S. R., Lozier, M. S., & Dunne, J. P. (2013). A comparison of methods to determine phytoplankton bloom initiation. *Journal of Geophysical Research: Oceans*, *118*(5), 2345–2357.

Cadiou, J.-F., Repecaud, M., Arnaud, M., Rabouille, C., Raimbaud, P., Radakovitch, O., ... Gaufrès, P. (2010). Mesurho: a high frequency oceanographic buoy at the rhone river mouth. In *39th ciesm congress-venice, italy, 10-14 may 2010.*

Finkel, Z. V., Beardall, J., Flynn, K. J., Quigg, A., Rees, T. A. V., & Raven, J. A. (2010). Phytoplankton in a changing world: cell size and elemental stoichiometry. *Journal of plankton research*, *32*(1), 119–137.

Marrec, P., Grégori, G., Doglioli, A. M., Dugenne, M., Della Penna, A., Bhairy, N., ... Thyssen, M. (2018). Coupling physics and biogeochemistry thanks to high-resolution observations of the phytoplankton community structure in the northwestern mediterranean sea. *Biogeosciences*, *15*(5), 1579–1606. Retrieved from `https://bg.copernicus.org/articles/15/1579/2018/` doi: 10.5194/bg-15-1579-2018

Menden-Deuer, S., & Lessard, E. J. (2000). Carbon to volume relationships for dinoflagellates, diatoms, and other protist plankton. *Limnology and oceanography*, *45*(3), 569–579.

Millot, C. (1979). Wind induced upwellings in the gulf of lions. *Oceanologica Acta*, *2*(3), 261–274.

Odic, R., Bensoussan, N., Pinazo, C., Taupier-Letage, I., & Rossi, V. (2022). Sporadic wind-driven upwelling/downwelling and associated cooling/warming along north-western mediterranean coastlines. *Continental Shelf Research (under final revision)*.

Ribalet, F., Swalwell, J., Clayton, S., Jiménez, V., Sudek, S., Lin, Y., ... Armbrust, E. V. (2015). Light-driven synchrony of prochlorococcus growth and mortality in the subtropical pacific gyre. *Proceedings of the National Academy of Sciences*, *112*(26), 8008–8012.

Sapiano, M., Brown, C., Schollaert Uz, S., & Vargas, M. (2012). Establishing a global climatology of marine phytoplankton phenological characteristics. *Journal of Geophysical Research: Oceans*, *117*(C8).

Sun, J., & Liu, D. (2003). Geometric models for calculating cell biovolume and surface area for phytoplankton. *Journal of plankton research*, *25*(11), 1331–1346.

Verity, P. G., Robertson, C. Y., Tronzo, C. R., Andrews, M. G., Nelson, J. R., & Sieracki, M. E. (1992). Relationships between cell volume and the carbon and nitrogen content of marine photosynthetic nanoplankton. *Limnology and Oceanography*, *37*(7), 1434–1446.

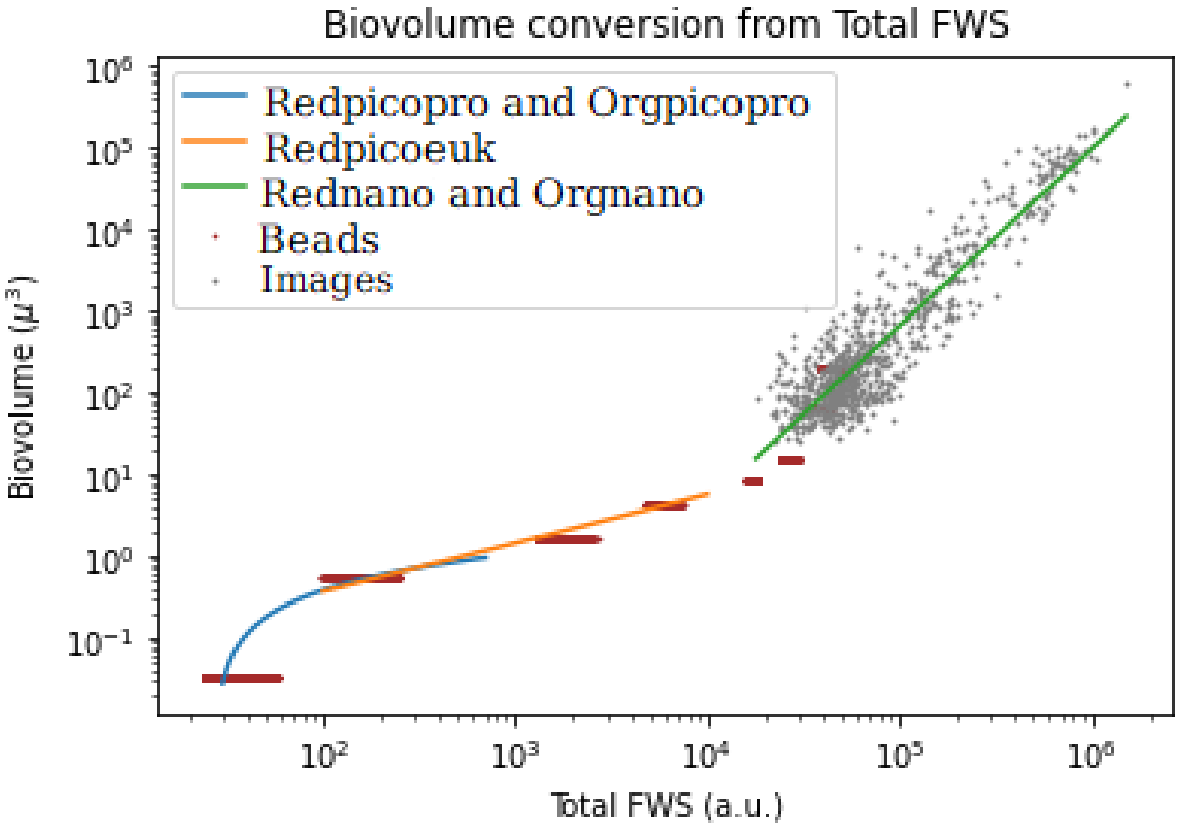

Figure S1. Summary of the empirical relationships used to convert the Total FWS signal of each cell into biovolume

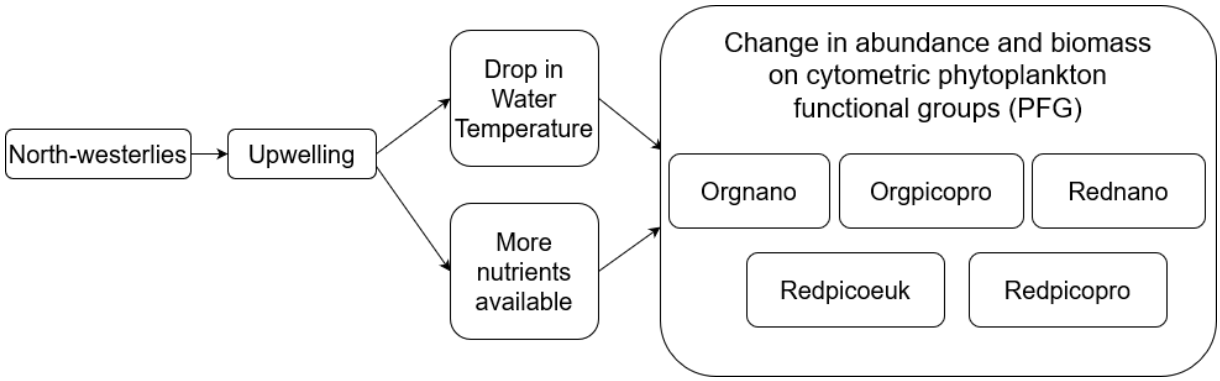

Figure S2. Summary of the causal relationships identified in this study. Reading of the underlying hydrodynamics: north-westerlies trigger offshore horizontal surface advection and upward vertical advection. Warm and nutrient-depleted surface water along with the associated phytoplankton (PFG) is exported offshore and replaced by deeper cold, nutrient-rich water, and the PFGs associated with these deeper water masses.

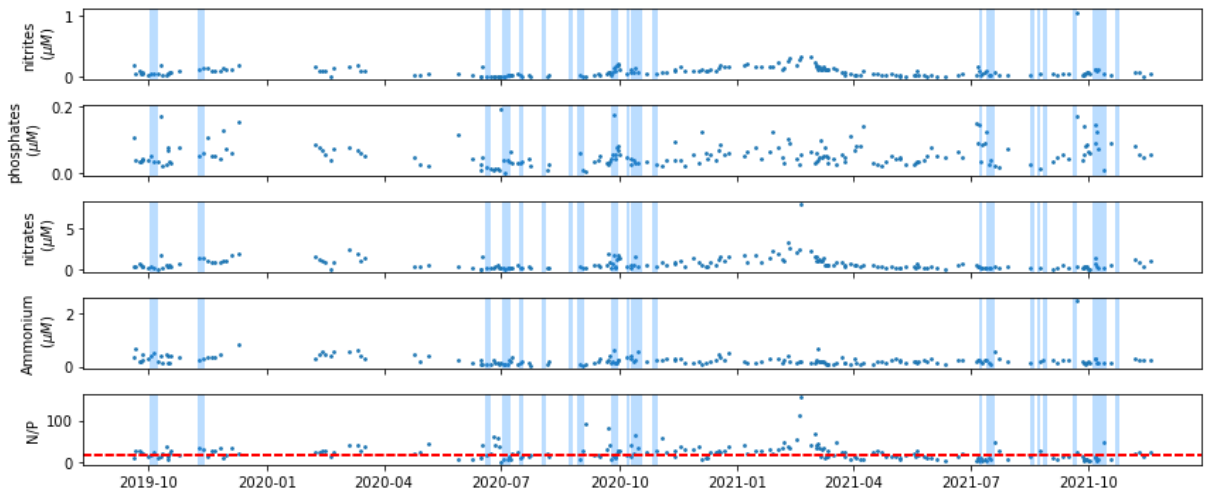

Figure S3. Nutrients over the two years of data. The colored rectangles correspond to the SWUEs considered in the study. The red dash line represent the N/P Redfield ratio (=16)

	Unstratified	Stratified Upwelling	Stratified Non SWUE
nitrites	0.10 (0.10)	0.05 (0.09)	0.03 (0.03)
phosphates	0.05 (0.03)	0.04 (0.04)	0.04 (0.04)
nitrates	0.90 (0.77)	0.26 (0.40)	0.36 (0.27)
Ammonium	0.22 (0.16)	0.20 (0.16)	0.19 (0.12)
N/P	25.15 (16.06)	17.33 (15.72)	13.06 (14.48)

Table S1. Medians and inter-quartile ranges (in parentheses) of the nutrients concentration (μM) for the nitrites, phosphates, nitrates, ammonium and N/P ratio during the unstratified periods, the SWUEs and unstratified period excluding SWUE.

	Unstratified	Stratified (SWUE reaction phase)	Stratified (Non SWUE)
Orgnano	4.03e-06 (6.74e-06)	2.55e-06 (2.87e-06)	3.66e-06 (5.23e-06)
Orgpicopro	1.55e-06 (2.38e-06)	2.16e-06 (1.55e-06)	3.12e-06 (2.49e-06)
Rednano	8.85e-06 (9.34e-06)	9.78e-06 (8.16e-06)	1.49e-05 (1.83e-05)
Redpicoeuk	1.64e-06 (2.11e-06)	9.37e-07 (1.03e-06)	6.52e-07 (6.88e-07)
Redpicopro	1.40e-07 (1.93e-07)	1.97e-07 (2.68e-07)	1.28e-07 (1.33e-07)

Table S2. Medians and inter-quartile ranges (in parentheses) of each PFG biomass (mgC.mL^{-1}) during the unstratified periods, the reaction of the PFG during SWUE, and in stratified periods outside of SWUEs.

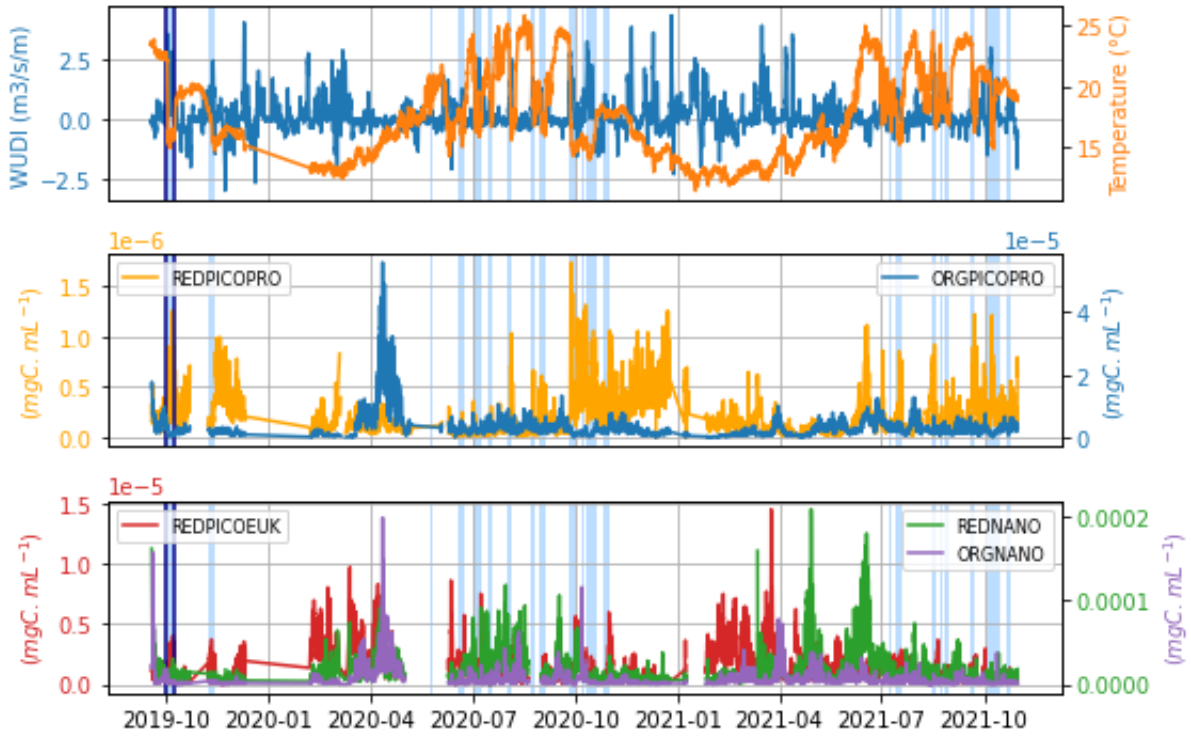

Figure S4. WUDI ($m^3.s^{-1}m^{-1}$) and temperature (C°) series (a), and phytoplankton biomass ($mgC.mL^{-1}$), at the SSL@MM station. The blue rectangles correspond to the studied SWUEs in the main text. The SWUE shown in Figure 2 in the main text is bounded by a dark blue box.

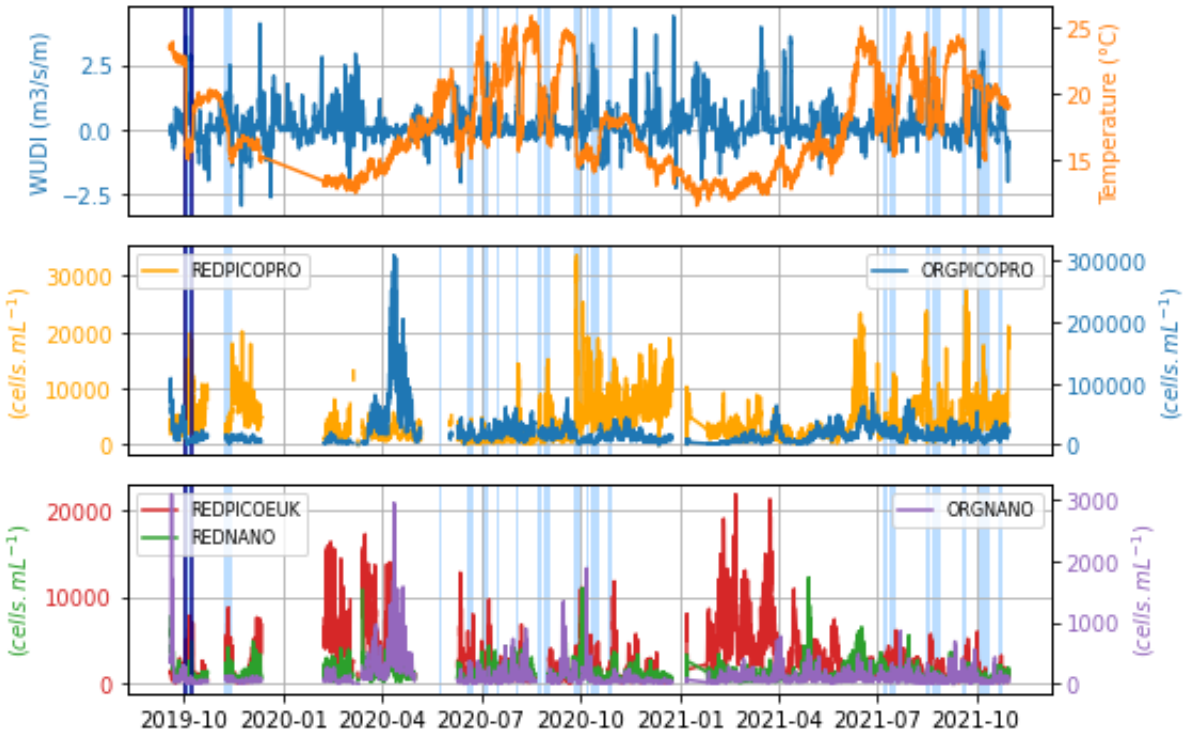

Figure S5. WUDI ($m^3.s^{-1}m^{-1}$) and temperature (C°) series (a), and phytoplankton abundances (cells.mL^{-1}), at the SSL@MM station. The blue rectangles correspond to the studied SWUEs in the main text. The SWUE shown in Figure 2 in the main text is bounded by a dark blue box.

	Unstratified	Stratified (SWUE reaction phase)	Stratified (Non-SWUE)
Orgnano	69.21 (97.68)	58.19 (62.24)	77.73 (90.02)
Orgpicopro	8706.83 (14998.82)	13161.05 (9739.31)	18633.22 (15789.77)
Rednano	881.50 (853.54)	908.64 (634.03)	1052.81 (1013.43)
Redpicoeuk	2775.45 (4229.14)	1612.28 (1866.72)	997.38 (1019.65)
Redpicopro	2734.51 (3167.50)	4267.94 (5349.91)	2988.55 (3747.08)

Table S3. Medians and inter-quartile ranges (in parentheses) of each PFG abundance (cells.mL^{-1}) during the unstratified periods, the reaction of the PFG during the SWUEs, and in stratified periods outside of SWUEs.

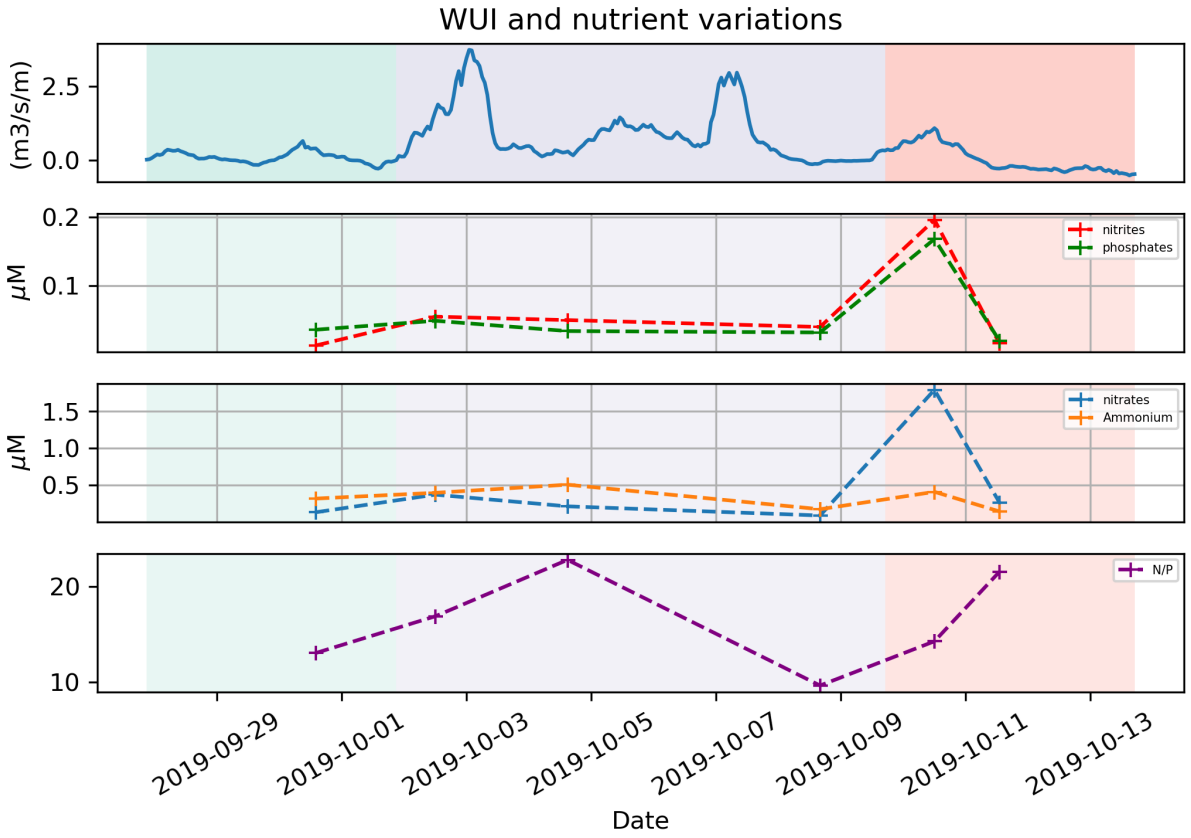

Figure S6. Nutrients and N/P ratio during the SWUE shown in Figure 2 in the main text.

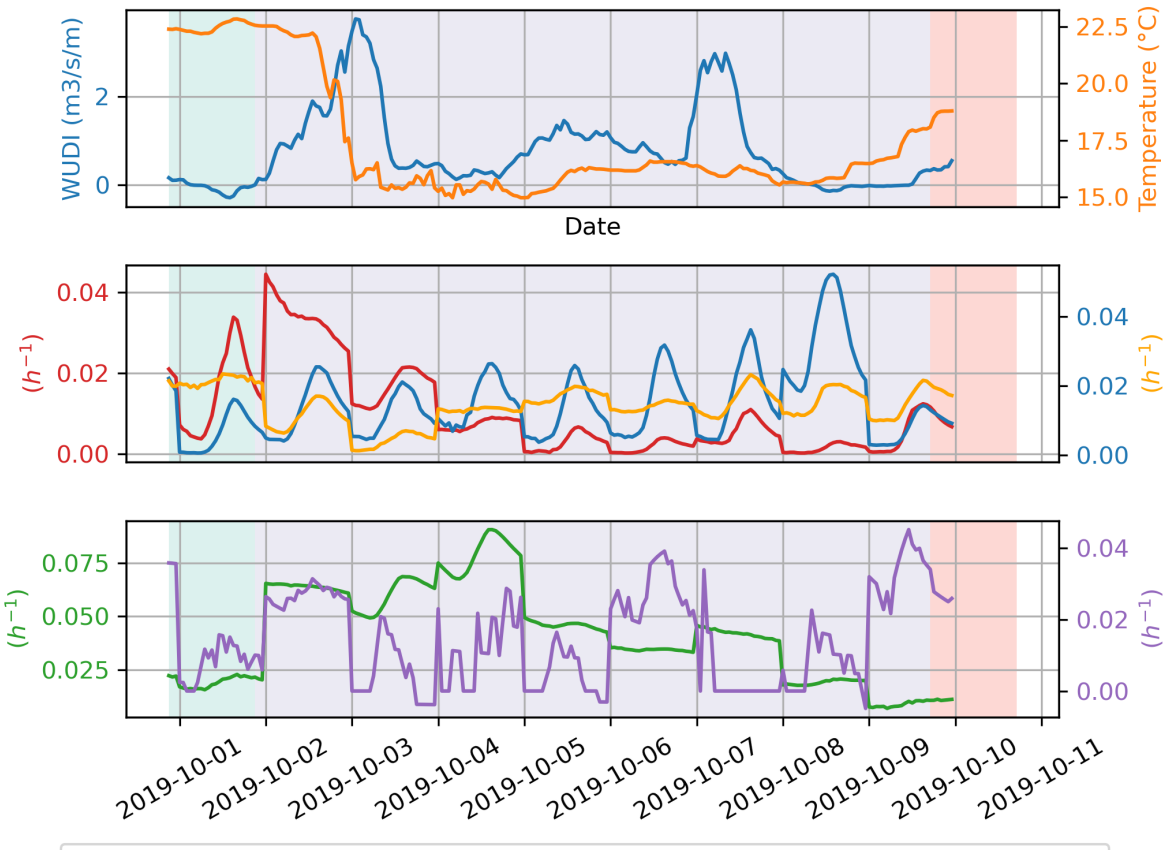

Figure S7. Hourly growth rates during the SWUE shown in Figure 2 in the main text.

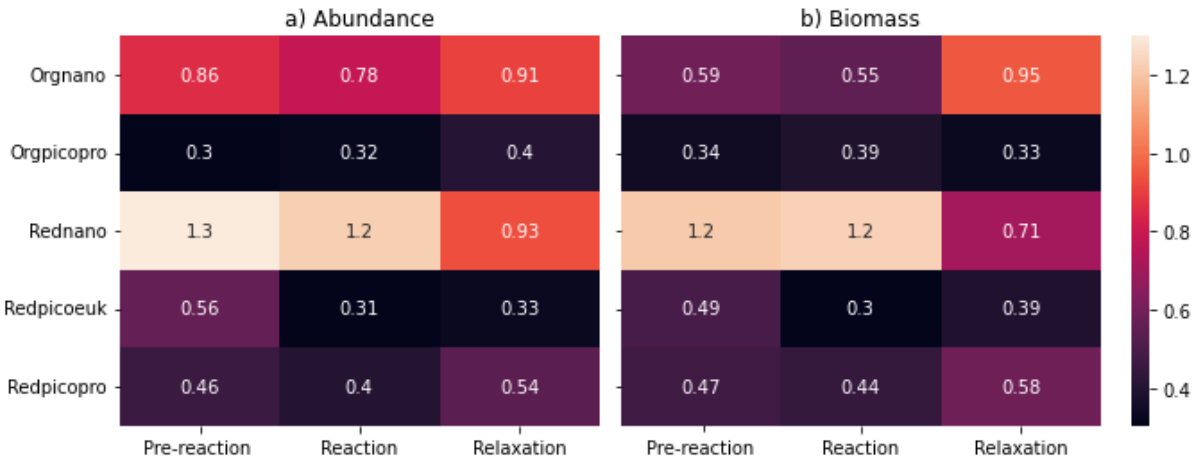

Figure S8. Estimated PFG daily growth rates during the three biological phases as defined by the abundance rupture points (a) or biomass rupture points (b). Only the Redpicoeuk growth rates significantly differed between the phases (for both abundance and biomass rupture points) and the Rednano using the biomass rupture points (Kruskal-Wallis test, p-value ≤ 0.05)

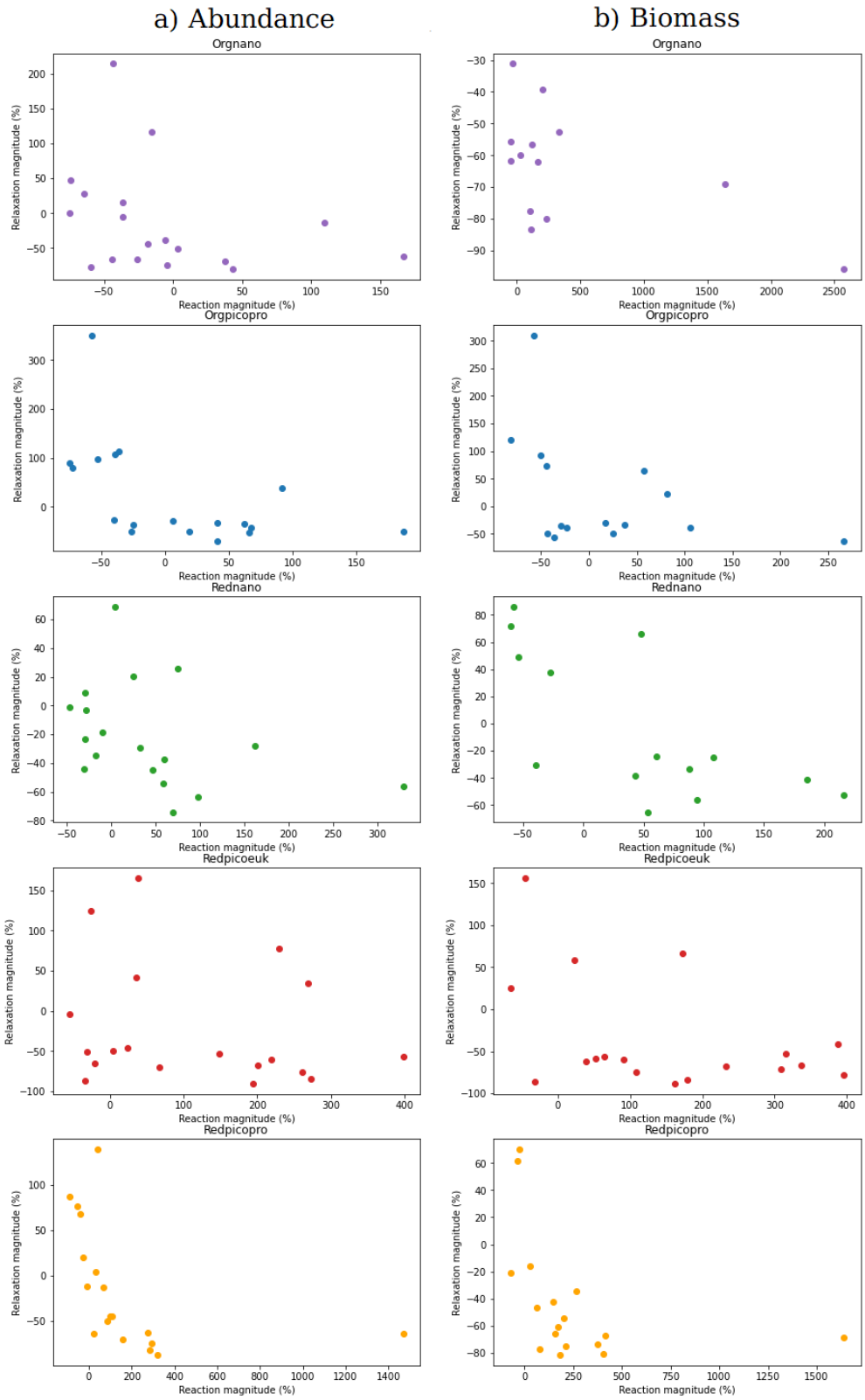

Figure S9. Inverse relationship existing between relaxation and reaction phases for all PFGs in both abundance (a) and biomass (b) illustrating a catch-up phenomenon.

Figure S10. Spearman correlations between estimated growth and loss rates using the abundance (a) and biomass (b) rupture points for all PFG before their reaction, during their reaction and during their relaxation phase. Only correlations significant at 5% are displayed. The number of observations on which these correlations are computed is given in Figure 3 in the main text.